

Supporting Information

for

Electronic Structure of the Quinone Radical Anion $A_1^{\bullet-}$ of Photosystem I Investigated by Advanced Pulse EPR and ENDOR Techniques

J. Phys. Chem. B.

Jens Niklas[†], Boris Epel[†], Mikhail L. Antonkine^{†,‡}, Sebastian Sinnecker[†], Maria-Eirini

Pandelia[†], and Wolfgang Lubitz^{,†}*

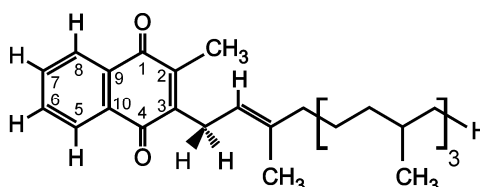
[†] Max-Planck-Institut für Bioanorganische Chemie, Stiftstrasse 34-36, 45470

Mülheim/Ruhr, Germany

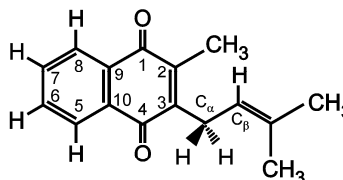
[‡] Institut für Experimentalphysik, Freie Universität Berlin, Arnimallee 14, 14195 Berlin,

Germany

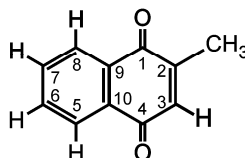
Vitamin K₁ (VK₁)



Vitamin K₁ (VK₁)
(truncated)



Vitamin K₃ (VK₃)



Plastoquinone-9 (PQ₉)

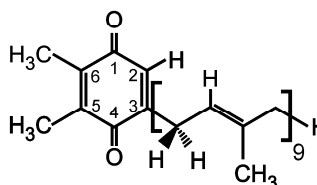


Figure S1. Molecular structure of vitamin K₁ (VK₁), the truncated vitamin K₁ model used for the DFT calculations (VK₁, truncated), vitamin K₃ (VK₃), and plastoquinone-9 (PQ₉). The numbering of the molecular positions is given. C_α and C_β denote the first and second carbon atom of the phytyl chain of VK₁.

Detailed Material and Methods Section

Quinone substitution and H/D exchange in the A₁ binding site of PS I

The quinone exchange in the A₁ binding site was performed in PS I isolated from *Synechocystis menB26*,¹ using fully protonated 2-methyl-1,4-naphthoquinone (VK₃-h₈) and fully deuterated 2-methyl-1,4-naphthoquinone (VK₃-d₈). The former was obtained commercially (Aldrich), while the latter was obtained from H. Zimmermann (MPI für Medizinische Forschung, Heidelberg, Germany). The comprehensive description of the preparation of VK₃-d₈ has been given previously.²

A two hundred fold molar excess of either VK₃-h₈ or VK₃-d₈ (30 mM solution in ethanol) was added to a 6-12 μM PS I solution (50 mM Tris pH 8.0 with 0.05% *n*-dodecyl-β-maltoside) isolated from *Synechocystis menB26* mutant cells. Incubation was carried out at

room temperature for 4 h with intensive stirring under room light and continued overnight in the dark at 4°C. Afterwards, the samples were washed twice with the same buffer to remove excess quinone using a 50 kDa Centricon and concentrated to a final volume of about 50 µL.

To achieve a H/D exchange in *Synechocystis menB26* PS I samples, a concentrated PS I solution (~1 mM Chl) was applied to a NAP-10 column equilibrated with D₂O-buffer (50 mM Tris pD 8.3, 0.05% *n*-dodecyl-β-maltoside), and eluted with the same deuterated buffer. Afterwards, the quinone exchange against VK₃-h₈ was performed as described above, but using the D₂O-buffer (50 mM Tris, pD 8.3, 0.05% β-DM). The sample was stirred overnight in the dark at 4°C to allow efficient exchange.

Preparation of PS I samples for EPR spectroscopy on the RP P₇₀₀^{•+} A₁^{•-}

Samples with PS I from *T. elongatus* and *Synechocystis menB26* contained between 0.1 and 0.2 mM PS I. Samples were reduced by adding sodium ascorbate solution (to a final concentration of 5 mM); after 5 minutes incubation in the dark at 4°C they were quickly frozen in liquid nitrogen in the dark.

Preparation of PS I samples for EPR spectroscopy on photoaccumulated A₁^{•-}

All steps were done under anaerobic conditions. The buffers were degassed and purged by argon. About 20 µL solution of trimeric PS I (> 12 mM Chl *a*) were mixed with 2.5 µL 1 M glycine buffer pH 10. Fresh sodium dithionite (Fluka, Neu-Ulm) was dissolved in 1 M glycine buffer pH 10 (final sodium dithionite concentration 300 mM), and 2.5 µL added to the PS I solution. This was followed by 30 minutes dark adaptation at 4°C, to ensure good pre-reduction of the iron-sulfur centers,³ and subsequent freezing. Illumination was carried out at 200 K by two 150 W halogen lamps from two sides. A water filter, cold glass filter

and a concentrated CuSO_4 solution were used to minimize IR and UV irradiation. The typical illumination time was 5 minutes. For PS I from *T. elongatus* an additional illumination for 10 minutes at 240 K was done. It was found that this increased the amount of $\text{A}_1^{\bullet-}$ considerably without yielding a significant amount of $\text{A}_0^{\bullet-}$.

EPR spectroscopy

All EPR and ENDOR experiments were carried out on a Bruker ELEXSYS E580 Q-band spectrometer with a Super Q-FT microwave bridge equipped with a home-built ENDOR resonator^{4,5}, similar to the one described previously.⁶ The resonator used for measurements of the light-induced RP $\text{P}_{700}^{\bullet+}\text{A}_1^{\bullet-}$ contained 12 horizontal slits of 0.3 mm width to allow *in situ* light excitation of the sample (>65% light transmission). Field-swept echo-detected (FSE) EPR spectra were recorded using the two-pulse echo sequence ($\pi/2$ - τ - π - τ -echo), in which the echo intensity was registered as a function of the external magnetic field. Microwave (MW) pulses of 40 ns ($\pi/2$) and 80 ns (π pulse) and $\tau = 400$ ns were used. The ^1H ENDOR spectra were recorded using the Davies ENDOR sequence⁷ (π - t - $\pi/2$ - τ - π - τ -echo) with an inversion π pulse of 200 ns, $t = 21$ μs , and radiofrequency (RF) π -pulse of 17 μs and the detection sequence similar to the FSE EPR experiment. One- and two-dimensional Davies TRIPLE experiments⁸⁻¹⁰ were performed using the same Davies-type ENDOR sequence as described above with the introduction of a second RF pulse of same length. An ENI 3200L (300W) RF amplifier or an AR2500L RF amplifier (Amplifier Research) were used for ^1H ENDOR/TRIPLE measurements. Light excitation at 532 nm was achieved with the Brilliant Laser system from Quantel. It consists of an OPO, type Vibrant 355 II, pumped by short (~ 8 ns) light pulses at 355 nm provided by a Nd:YAG Laser. The light was coupled into the cavity by an optical fiber with output energy of ~ 12 mJ. Field-sweep echo-detected (FSE) EPR and ENDOR spectra were recorded as

described above. The **Delay After laser Flash (DAF)** was 1 μ s. For ^1H ENDOR measurements of the RP the generation of RF pulses and the detection was done by an external PC equipped with the SpecMan program¹¹ and an Agilent E4420B RF synthesizer. The sequence of MW and RF pulses and the detection was repeated twice 10 ms and 20 ms after the Laser flash, to allow subtraction of stationary background signals. An ENI 3200L 300W RF amplifier was used for these measurements. The **Variable Mixing Time (VMT)** ENDOR experiment^{12;13} on the RP¹⁴ was similar to the Davies type ENDOR experiment. An AR2500L RF amplifier (Amplifier Research) was used. Details of the VMT ENDOR experiments have been described previously.¹⁴ All pulse EPR and ENDOR spectra of the RP were corrected for the stationary background spectra recorded 10 ms after the Laser flash.

Transient Q-band EPR measurements of the RP $\text{P}_{700}^{\bullet+}\text{A}_1^{\bullet-}$ were done with the same spectrometer using the direct detection method.¹⁵⁻¹⁷

Spectral simulations

Stationary radicals

The spin Hamiltonian for the case of an electron spin $S = 1/2$ and nuclear spins I_i has the form

$$H = \mu_B \vec{B}_0 \mathbf{g} \vec{S} + \sum_{i=1}^n \left(-\mu_N^i g_N^i \vec{B}_0 \vec{I}_i + \vec{S} \mathbf{A}_i \vec{I}_i + \vec{I}_i \mathbf{Q}_i \vec{I}_i \right), \quad (\text{Eq. S1})$$

where B_0 is the external magnetic field, \mathbf{g} is the electronic g -tensor, \mathbf{A}_i and \mathbf{Q}_i correspond to the hyperfine (hfc) and quadrupole (nq) tensors of nucleus i , respectively. μ_B is the Bohr magneton, μ_N and g_N are the nuclear magneton and g -factor of corresponding nuclei. For nuclei with spin $I = 1/2$ the quadrupolar term in Eq. S1 is zero. The frequencies and probabilities of EPR and ENDOR transitions are derived from Eq. S1 by application of the

selection rules $\Delta M_S = 1$ and $\Delta M_I = 0$, and $\Delta M_S = 0$ and $\Delta M_I = 1$ for allowed EPR and ENDOR transitions, respectively. Since paramagnetic centers of a frozen solution sample are randomly oriented, the EPR spectra are obtained by summation of signals from all orientations. For the correct calculation of the EPR spectra the strongly coupled protons were included. The ENDOR experiments are performed at a specific magnetic field. Due to the finite width of the microwave pulses, only part of the EPR spectrum is excited. This effect (orientation selection) has to be taken into account to correctly estimate the impact of different transitions on the final ENDOR spectra.¹⁸⁻²⁰ The orientation selectivity of MW pulses in ENDOR was accounted for by i) inclusion of the strongly coupled protons in the spin Hamiltonian, ii) manual specification of the excitation width of pulses, comparable with the EPR linewidth. All data processing routines and simulations were done in MatlabTM environment.²¹ EPR spectra were simulated using the EasySpin software package (version 2.7.1).²² For ENDOR and TRIPLE simulations the EasySpin package together with home-written routines was used. Both EPR and ENDOR simulations were done simultaneously to increase the precision of the determination parameters. The ENDOR signatures of every nucleus were obtained separately and then summed with appropriate weight coefficients. A manual fit of experimental data was used in all cases.

The spin-polarized RP $P_{700}^{\bullet+}A_1^{\bullet-}$

The simulations of the EPR spectra of the spin-polarized radical pair $P_{700}^{\bullet+}A_1^{\bullet-}$ were done with the program of Salikhov and coworkers²³⁻²⁵ (in MatlabTM environment²¹). The protons of the methyl group were included in the simulation.

Simulations of the ENDOR spectra of the spin-polarized RP $P_{700}^{\bullet+}A_1^{\bullet-}$ were done using similar procedures as for stationary radicals.²

DFT calculations of VK₁^{•-} and VK₃^{•-} in the A₁ binding site (A-branch)

The coordinates of the A-branch A₁ binding site were taken from the X-ray crystal structure of PS I from *T. elongatus* (PDB entry 1JB0).²⁶ DFT calculations were performed for two different model systems, the first containing the quinone VK₁ (with a truncated phytyl chain; Figure S1), and the second one containing the quinone VK₃ (Figure 1 or S1). In case of VK₃ in the A₁ binding site the same starting structure was chosen, while the phytyl chain was replaced by a hydrogen atom.

The smallest feasible system of the protein surrounding was chosen. It has been shown previously, that hydrogen bonding to quinones has to be explicitly taken into account in DFT calculations, since it has considerable influence on the electronic structure of the quinone.^{2,4;27-35} The peptide nitrogen of the leucine residue PsaA-L722 is involved in hydrogen bonding to the quinone oxygen O₄. Hence, this leucine and the alanine (PsaA-A721) preceding it was partially included. The side chain of the leucine residue was replaced by a methyl group, while the NH₂ and the CH₃ groups of the alanine were replaced by hydrogen atoms (see Figure 5). Other nearby residues were not included, since the interactions between them and the quinone are assumed to be of less importance.

A restricted geometry optimization was performed for both model systems. The orientation of the leucine with respect to the quinone was kept frozen, while the H-bond length was not fixed. This was realized by fixing (i) the distance between the carbonyl oxygen O₄ and the leucine nitrogen atom, (ii) the angle between C₄, O₄, and the leucine nitrogen atom, and (iii) the dihedral angle between C₃, C₄, O₄, and the leucine nitrogen atom. In addition, the orientation of the phytyl chain was fixed in case of VK₁ (the dihedral angle C_β-C_α-C₃-C₂ was kept constant, see Figure S1). All other geometrical parameters were fully optimized. The B3LYP density functional³⁶⁻³⁸ was used in combination with the Dunning-Huzinaga basis set, which was augmented by polarization and diffuse functions

from the same authors.³⁹ Geometry optimizations were performed with the Gaussian 03 program.⁴⁰ Additional restricted geometry optimizations were performed for the same model systems containing neutral quinones.

The optimized geometries obtained were the input for single point calculations, which provided the spectroscopic parameters. These calculations were performed with the program package ORCA.⁴¹ The B3LYP functional was used in combination with the EPR-II basis set, which was developed for an accurate calculation of magnetic properties.⁴² The *g*-values were calculated employing the coupled-perturbed Kohn-Sham equations,⁴³ in conjunction with a parameterized one electron spin-orbit operator.⁴⁴⁻⁴⁶ The magnetic dipole and the isotropic Fermi contact hfc were calculated for all atoms. To account for the rotation of the methyl groups, additional single point calculations were performed with several methyl group rotation angles. All raw hyperfine matrices obtained were summed; afterwards, the eigenvectors and eigenvalues were determined. DFT single point calculations were also performed using COSMO⁴⁷ to account for dielectric screening effects of the protein surrounding.

Expanded Results Section

The spin-polarized RP $P_{700}^{\bullet+} A_1^{\bullet-}$

The principal g -values obtained from simulation of the transient EPR spectra (data not shown) are given in Table S1. The principal g -values obtained from simulation of the pulse EPR spectra of photoaccumulated $A_1^{\bullet-}$ in PS I from *T. elongatus* are also provided. They are in good agreement with the g -values determined in several previous studies.⁴⁸⁻⁵³

Table S1. Principal g -values of the photoaccumulated radical anion $A_1^{\bullet-}$ (values in parentheses) and $A_1^{\bullet-}$ in the RP $P_{700}^{\bullet+} A_1^{\bullet-}$.

	Quinone	g_x	g_y	g_z	g_{iso}
<i>T. elongatus</i>	VK ₁	(2.0063)	(2.0051)	(2.0023)	(2.0046)
		2.0062	2.0051	2.0022	2.0045
<i>Syn. menB</i> mutant	PQ ₉	2.0067	2.0051	2.0022	2.0047
<i>Syn. menB</i> mutant	VK ₃ -d ₈	2.0063	2.0051	2.0024	2.0046
<i>Syn. menB</i> mutant	VK ₃ -h ₈	2.0063	2.0051	2.0024	2.0046
DFT on A_1 (H-bonded)	VK ₁ (truncated)	2.0073	2.0055	2.0022	2.0050
DFT on A_1 (H-bonded)	VK ₃	2.0073	2.0050	2.0022	2.0048

The error in the determination of the principal g -values is ± 0.00015 . The g -tensor of $P_{700}^{\bullet+}$ ($g_x = 2.0031$, $g_y = 2.0026$, $g_z = 2.0023$) and the interaction tensor ($D = 170 \mu\text{T}$, $J = 1 \mu\text{T}$) are the same as determined previously.⁴⁸ The principal axes of the g -tensor are expected to be collinear with the molecular axes system given in Figure 1c.

In Figure S2 the pulse Q-band EPR spectra and ¹H ENDOR spectra of $A_1^{\bullet-}$ in photoaccumulated samples (a) and in RP samples (b) of PS I from *T. elongatus*, and of RP samples of PS I from *Synechocystis menB26* substituted with VK₁ (c), VK₃-h₈ (d), VK₃-d₈ (e), and PQ₉ (f) in the A_1 binding site are presented. The spectral positions at which the ENDOR spectra were recorded are marked in the respective EPR spectrum.

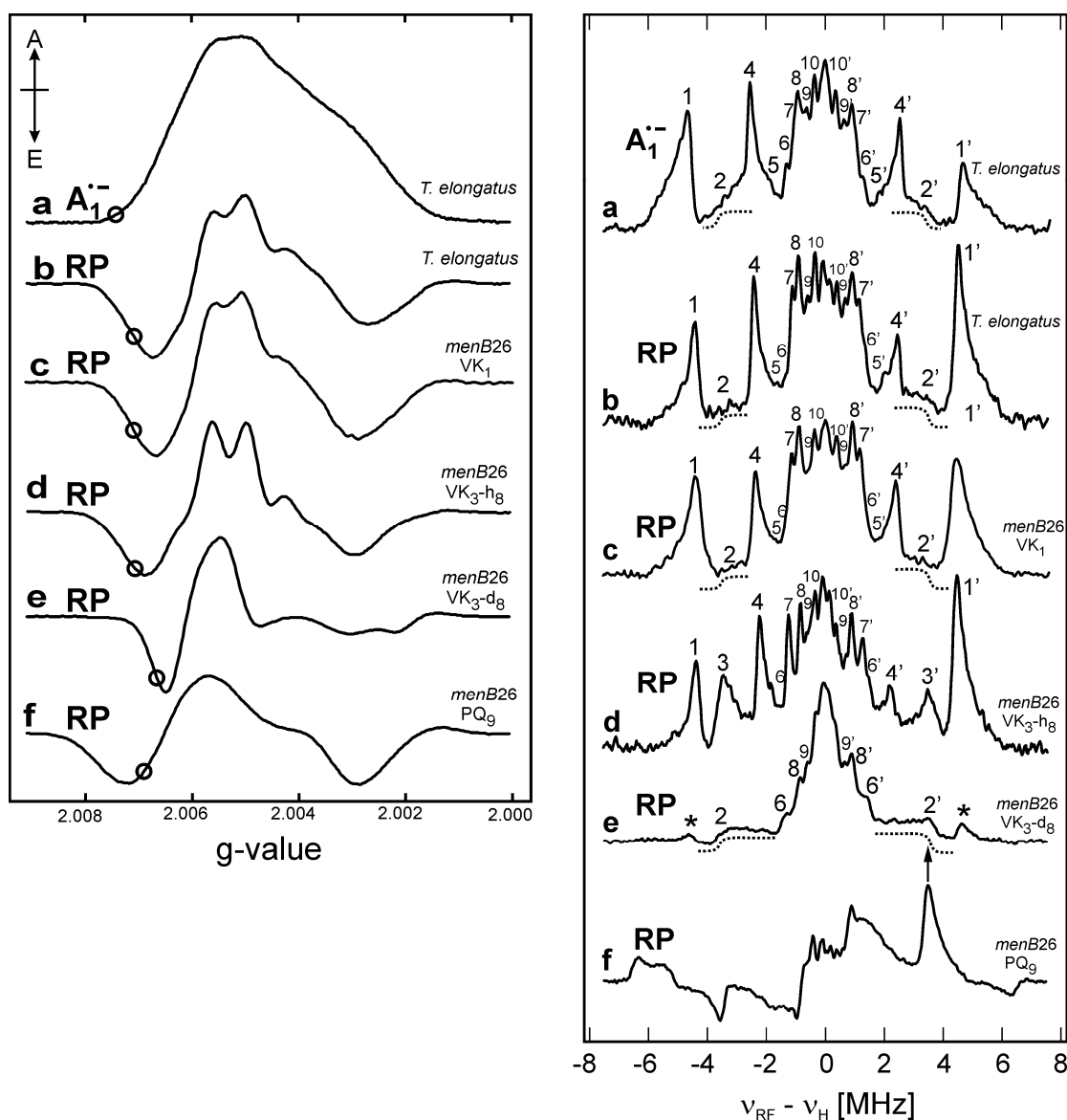


Figure S2: Pulse Q-band EPR (left) and 1H ENDOR spectra (right) recorded at the low field edge of the EPR spectrum of $A_1^{\bullet-}$ in photoaccumulated and RP PS I samples. The spectral positions at which the ENDOR spectra were recorded are marked in the respective EPR spectrum. The largest component of the H-bond proton signal ($A_{||}$) is marked by a dotted line for better visualization. Note that the ENDOR spectra of the RP samples are only presented as absorptive ENDOR lines to facilitate comparison with the ENDOR spectrum of the photoaccumulated radical anion. (a) Photoaccumulated $A_1^{\bullet-}$ in *T. elongatus* PS I; (b) RP in *T. elongatus* PS I; (c) RP in PS I from *Synechocystis menB26* with VK_1 in the A_1 binding site; (d) RP in *menB* mutant PS I with VK_3-h_8 in the A_1 binding site; (e) RP in PS I from *Synechocystis menB26* with VK_3-d_8 in the A_1 binding site; (f) RP in PS I from *Synechocystis menB26* with PQ_9 in the A_1 binding site. The signals of the impurity (from ~3% non-deuterated VK_3) are marked with asterisks.

The chlorophyll radical anion $A_0^{\bullet-}$

As described previously, the stationary radical anion $A_1^{\bullet-}$ can be generated by the photoaccumulation procedure.^{54;55} The PS I complexes are treated with sodium dithionite (a reducing agent), are subsequently incubated at 4°C in the dark for 30 minutes, and then frozen. This treatment leads to a partial reduction of the FeS-clusters, but not of A_1 .³ The illumination of the frozen sample results in charge separation; in the charge separated state, the radical cation $P_{700}^{\bullet+}$ can be reduced by the reductant, if the temperature is not too low (≥ 200 K). This leads to the generation of a stationary radical anion $A_1^{\bullet-}$ (termed also photoaccumulated $A_1^{\bullet-}$). To obtain a sufficient amount of $A_1^{\bullet-}$ in the sample, the illumination takes usual several minutes. The charge separation in PS I complexes, with a photoaccumulated radical anion $A_1^{\bullet-}$ already present, can lead to the generation of the Chl radical anion $A_0^{\bullet-}$, which precedes A_1 in the electron transfer chain.^{54;56;57} Hence, it is vital for a thorough analysis of the ^1H ENDOR spectra of photoaccumulated $A_1^{\bullet-}$, to (i) to minimize the amount of $A_0^{\bullet-}$ in the $A_1^{\bullet-}$ samples and (ii) to identify ^1H ENDOR lines that belong to the Chl radical anion $A_0^{\bullet-}$.

Previous ^1H ENDOR studies on $A_0^{\bullet-}$ in PS I samples from several organisms have shown, that some hfcs of $A_0^{\bullet-}$ are larger than any of the hfcs of $A_1^{\bullet-}$.⁵⁸⁻⁶¹ These lines can therefore be considered as markers for the presence of $A_0^{\bullet-}$. A variety of ENDOR lines arising from protons with smaller hfcs, which overlap with the ENDOR lines of $A_1^{\bullet-}$, has also been reported.⁵⁸⁻⁶¹ We performed ENDOR measurements on several photoaccumulated PS I samples under the same experimental conditions which were used for the ENDOR experiments on photoaccumulated $A_1^{\bullet-}$.

EPR and ENDOR spectra were recorded on two samples of *T. elongatus* PS I using different photoaccumulation conditions. The first sample was illuminated only 5 minutes using the illumination setup mentioned above. These conditions should result in an almost pure $A_1^{\bullet-}$ sample.

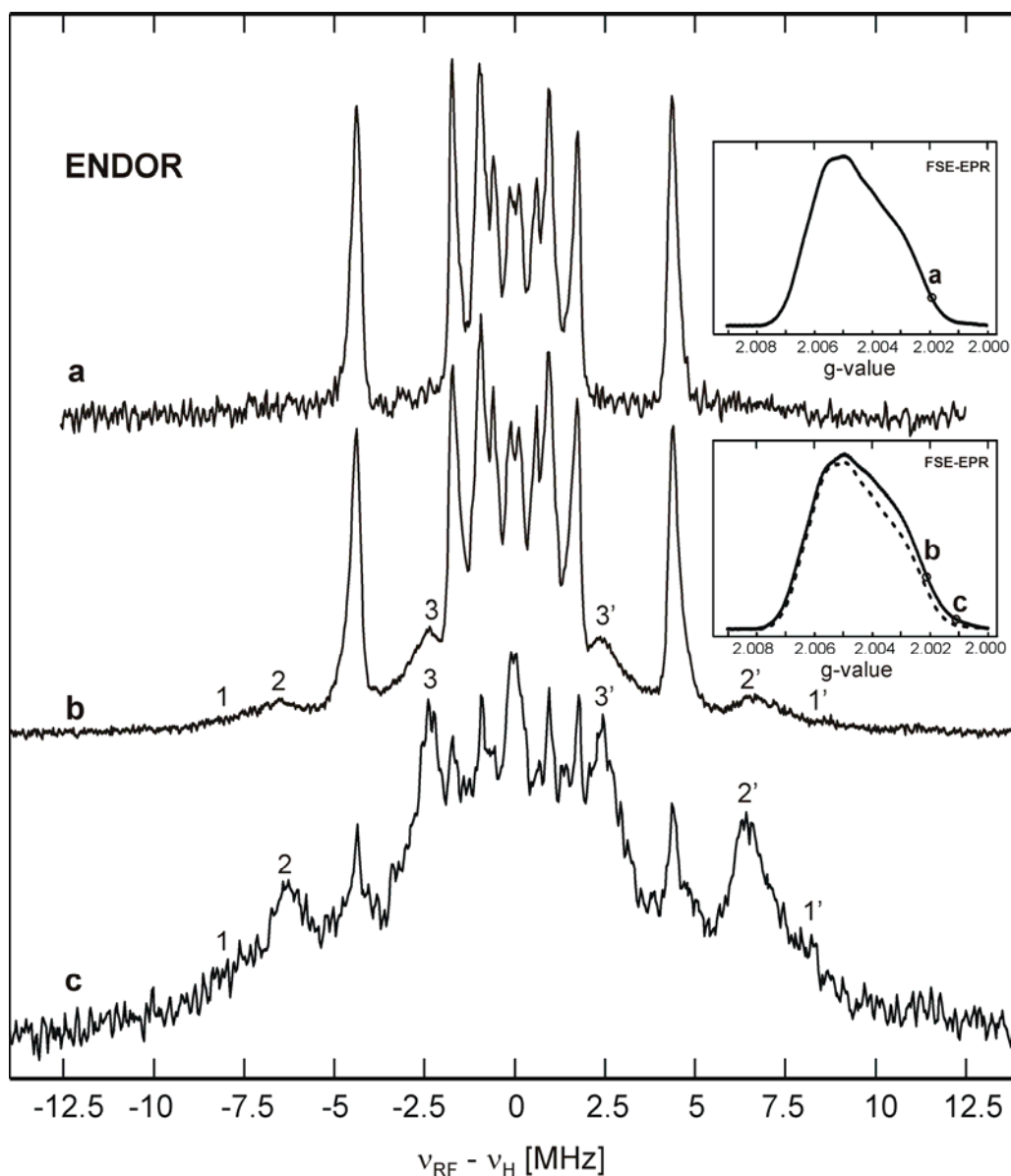


Figure S3. Comparison of pulse Q-band ^1H ENDOR spectra recorded on different photoaccumulated PS I samples from *T. elongatus* ($T = 80\text{ K}$). The top insert shows the FSE detected EPR spectrum of the ‘pure’ $A_1^{\bullet-}$ sample. The bottom insert shows the FSE detected EPR spectrum of the sample with an $A_1^{\bullet-}/A_0^{\bullet-}$ mixture (solid line). For comparison, the EPR spectrum of (a) is also shown (dashed line). The field positions, at which the presented ENDOR spectra were measured, are marked with letters. (a) $A_1^{\bullet-}$ in *T. elongatus* PS I (close to the g_z spectral position, see insert); (b) $A_1^{\bullet-}/A_0^{\bullet-}$ mixture in *T. elongatus* PS I (close to the g_z spectral position, see insert for position); (c) $A_1^{\bullet-}/A_0^{\bullet-}$ mixture in *T. elongatus* PS I (same sample as b), see insert for position)

The ENDOR spectrum of this sample, recorded close to the g_z spectral position, is shown in Figure S3, spectrum (a). The second PS I sample was chemically treated identically but illuminated without glass filters (higher light intensity) at 240 K for 30 minutes. Under these conditions an accumulation of $A_0^{\bullet-}$ additional to $A_1^{\bullet-}$ is likely.⁵⁴ The comparison of the Q-band EPR spectra of these two samples (see bottom insert of Figure S3) confirms the presence of an additional photoaccumulated radical in the PS I sample. The subtraction of the two EPR spectra results in an inhomogeneously broadened EPR line ($LW_{\text{fwhm}} \sim 22$ G, $g \sim 2.0037$, not shown). This is typical for Chl *a* anion radicals like $A_0^{\bullet-}$.^{54;58;61;62}

An ENDOR spectrum of this sample recorded close to the g_z spectral position is shown in Figure S3, spectrum (b). This spectrum closely resembles (a), but shows three additional ENDOR line pairs (numbered 1/1', 2/2', and 3/3'). Spectrum (c) in Figure S3 shows the ENDOR spectrum at a magnetic field, where the contribution of $A_1^{\bullet-}$ is expected to be very small, while $A_0^{\bullet-}$ will still show some contribution to the ENDOR spectrum due to its larger EPR linewidth (see Figure S3, bottom insert). The ENDOR lines of $A_1^{\bullet-}$ are present, but exhibit quite low intensity. In contrast, the three line pairs visible in spectrum (b) are dominating the ENDOR spectrum (c). The comparative analysis of the three ENDOR spectra clearly identifies these three line pairs being due to the presence of $A_0^{\bullet-}$.ⁱ Line pair 1/1' is very broad. The more narrow line pair (2/2') is due to protons with a hfc in the range of 13 MHz, probably from methyl groups of the Chl *a* molecule.^{58;61} One quite intense line pair (3/3') with a hfc of about 4.8 MHz is also observed. Lines arising from more weakly coupled protons overlap with the residual, but narrow single-crystal-like ENDOR signals of

ⁱ It should be noted, that during the photoaccumulation procedure also other chlorophyll molecules might be reduced and contribute to the EPR and ENDOR spectra. Under our experimental conditions they are probably indistinguishable from $A_0^{\bullet-}$.

$A_1^{\bullet-}$. Further measurements on various PS I samples from different organisms and preparation were also performed, and will be discussed in a future paper.⁶³

From our analysis it can be concluded, that $A_0^{\bullet-}$ contamination in PS I from *T. elongatus* manifests itself mainly with a broad line pair with hfcs of about 13 MHz, and at least one more narrow and intense line pair (3/3') with hfcs about 4.8 MHz, and the $A_1^{\bullet-}$ sample from *T. elongatus* PS I used in this work contains a negligible amount of $A_0^{\bullet-}$.

The attempts to prepare photoaccumulated $A_1^{\bullet-}$ samples using PS I from *Synechocystis menB26* substituted with VK₃-h₈ and VK₃-d₈ with a negligible amount of $A_0^{\bullet-}$ were not successful. A severe contribution of $A_0^{\bullet-}$ was always observed (data not shown). This was already previously found for this mutant.^{53;64} In fact, even photoaccumulated samples of PS I from *Synechocystis* sp. PCC 6803 wild type also contained a small amount of $A_0^{\bullet-}$.⁶³ Only from PS I isolated from *T. elongatus*, $A_1^{\bullet-}$ samples could be prepared with a negligible amount of $A_0^{\bullet-}$. However, as shown above, also in PS I from this organism a significant amount of $A_0^{\bullet-}$ can be created under certain experimental conditions. This apparent problem with $A_0^{\bullet-}$ contamination in quinone substituted samples could only be circumvented by the use of RP samples. In several previous ENDOR studies of photoaccumulated $A_1^{\bullet-}$, low intensity signals arising from protons with hfcs in the range of 12-14 MHz and 4.8 MHz were assigned to the H-bond proton in $A_1^{\bullet-}$.^{53;65-70} In view of the findings presented here, those assignments have to be critically re-considered. This is discussed in detail in the main article in the discussion section related to the H-bond.

Determination of the signs of hyperfine coupling constants

The signs of hfcs represent essential information about the spin system. Two different methods for the determination of hfc signs were used in this: **V**ariable **m**ixing **t**ime (VMT) ENDOR¹²⁻¹⁴ experiments were performed on the RP $P_{700}^{\bullet+}A_1^{\bullet-}$, while electron-nuclear-nuclear triple resonance (TRIPLE)⁸⁻¹⁰ was used for the photoaccumulated $A_1^{\bullet-}$.

Variable **M**ixing **T**ime (VMT) ENDOR measurements on the RP

Variable **M**ixing **T**ime (VMT) ENDOR experiments were performed to determine the absolute signs of the proton hfcs. This relaxation based method has been described in detail in our previous paper.¹⁴ It is based on the strong non-Boltzmann population of the electronic levels in the spin-polarized RP and the different life times of the electronic levels. Directly after creation of the RP $P_{700}^{\bullet+}A_1^{\bullet-}$ only the electronic states that carry some singlet character are populated.^{71;72} These levels decay faster than the electronic states with have only triplet character. This was also found the spin-polarized RP in bacterial photosynthetic reaction centers.^{73;74} In a VMT ENDOR experiment, the detection part of the Davies ENDOR sequence is shifted away from the RF pulse (Figure S4) by a time t_{mix} , which is in the order of the decay of the faster decaying RP states (some tens of μs). As a result ENDOR transitions of a nucleus in the fast decaying state become less intense as compared to ENDOR transitions in the slow relaxing state. For the RP $P_{700}^{\bullet+}A_1^{\bullet-}$ at Q-band this approximation is only valid for the low field edge. This means for a proton ($g_N > 0$) in the weak hyperfine coupling limit ($|A/2| < \nu_H$): (i) the ENDOR spectrum is symmetric around ν_H , (ii) all ENDOR lines exhibit the same polarization (emissive, since the EPR signal is also emissive). In the VMT experiment the low frequency ENDOR transition of a proton with a positive hfc will be more diminished in amplitude than the high frequency ENDOR transition. For a proton with a negative hfc the ENDOR amplitude will behave in the

opposite fashion. A RP VMT ENDOR experiment on *T. elongatus* PS I is shown in Figure S4. It is particularly useful when applied at spectral positions where only $A_1^{\bullet-}$ is observed with purely emissive or absorptive ENDOR spectra. At the low field wing single crystal-like ENDOR spectra are observed, which show only emissive ENDOR lines. Hence, this magnetic field position is well suited for the VMT experiment.

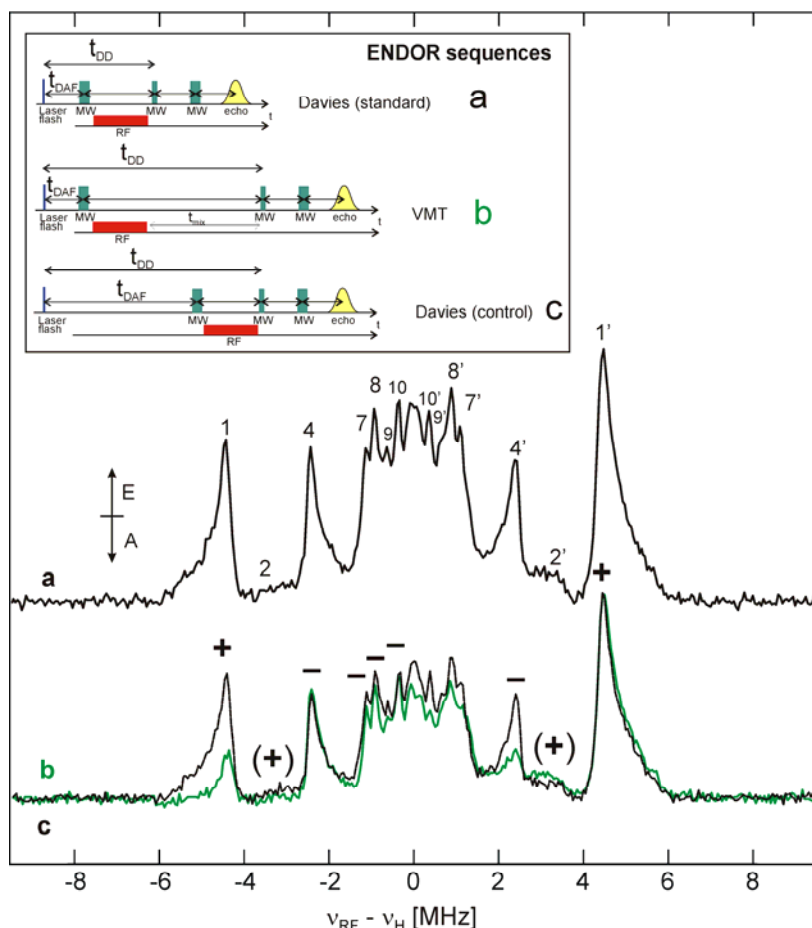


Figure S4. Variable mixing time (VMT) pulse Q-band ^1H ENDOR spectra recorded at the low field edge on the RP in PS I from *T. elongatus* ($T = 80\text{ K}$). t_{DAF} = delay after Laser flash, t_{DD} = delay after the Laser Flash to the beginning of the detection sequence, t_{mix} = time after the end of the RF pulse to the beginning of the detection sequence.). The insert shows schematically the three sequences used to obtain the spectra. For details, see ref. ¹⁴. E = emission, A = absorption. (a) Standard Davies ENDOR spectrum recorded with $t_{\text{DAF}} = 1\text{ }\mu\text{s}$ and a delay of $3\text{ }\mu\text{s}$ between the end of the RF pulse and the detection sequence ($t_{\text{DD}} = 14\text{ }\mu\text{s}$). The numbering of the lines is the same as in Figure S2. (b) **Green spectrum:** VMT ENDOR spectrum recorded with $t_{\text{DAF}} = 1\text{ }\mu\text{s}$ and a delay of $43\text{ }\mu\text{s}$ (t_{mix}) between the end of the RF pulse and the detection sequence ($t_{\text{DD}} = 54\text{ }\mu\text{s}$). (c) Black spectrum: Davies ENDOR spectrum recorded with $41\text{ }\mu\text{s}$ DAF and a delay of $3\text{ }\mu\text{s}$ between the end of the RF pulse and the detection sequence ($t_{\text{DD}} = 54\text{ }\mu\text{s}$). The signs of the hfcs of selected lines are given on the spectrum (b).

Spectrum **(a)** shows a ENDOR spectrum using the standard Davies ENDOR sequence ($t_{\text{DAF}} = 1 \mu\text{s}$, $t_{\text{DD}} = 14 \mu\text{s}$). The black spectrum **(b)** (control) was recorded with the same sequence as in spectrum **(a)**, but t_{DAF} was increased from $1 \mu\text{s}$ to $41 \mu\text{s}$ ($t_{\text{DAF}} = 41 \mu\text{s}$, $t_{\text{DD}} = 54 \mu\text{s}$). For the green spectrum **(b)** the $3 \mu\text{s}$ delay was increased to $43 \mu\text{s}$ ($t_{\text{DAF}} = 1 \mu\text{s}$, $t_{\text{DD}} = 54 \mu\text{s}$). All other parameters like MW and RF pulses were kept the same for all measurements. The spectra **(a)** and **(b)** are essentially the same spectrum. The hfcs in the ENDOR spectra are not dependent on t_{DD} (this was found for all PS I samples investigated here). Spectrum **(b)** exhibits, however, marked intensity changes. Line pair 1/1' shows the VMT induced asymmetry characteristics for protons with positive hfc (less intense low-frequency line). In case of line pair 2/2' only a weak effect is observed. This may be due to different relaxation times. The opposite behavior as for the line pair 1/1' is found for the line pair 4/4', which indicates a negative sign of the hfc. This corroborates the assignment of this hfc to an α -proton of the benzene ring. The inner lines show less pronounced effects. The overlap with signals from protons with different signs of the hfcs probably causes this problem. However, a careful analysis reveals that the hfcs of the protons associated with the (narrow) signals 7/7', 8/8' and 10/10' have negative signs.

A closer inspection of spectrum **(a)** shows already here some intensity asymmetry for signals originating from hfcs with different signs. It can be concluded that the relatively long time of the RF pulse ($9 \mu\text{s}$) already induces a VMT-type intensity asymmetry in the 'normal' ENDOR spectrum. This is even more prominent for all other ENDOR spectra that were recorded with longer ($17 \mu\text{s}$) RF pulses.

VMT ENDOR experiments were performed on the low field edge of the RP of *Synechocystis menB26* PS I substituted with VK₃-h₈ and VK₃-d₈ as well (Figures S5 and S6, respectively).

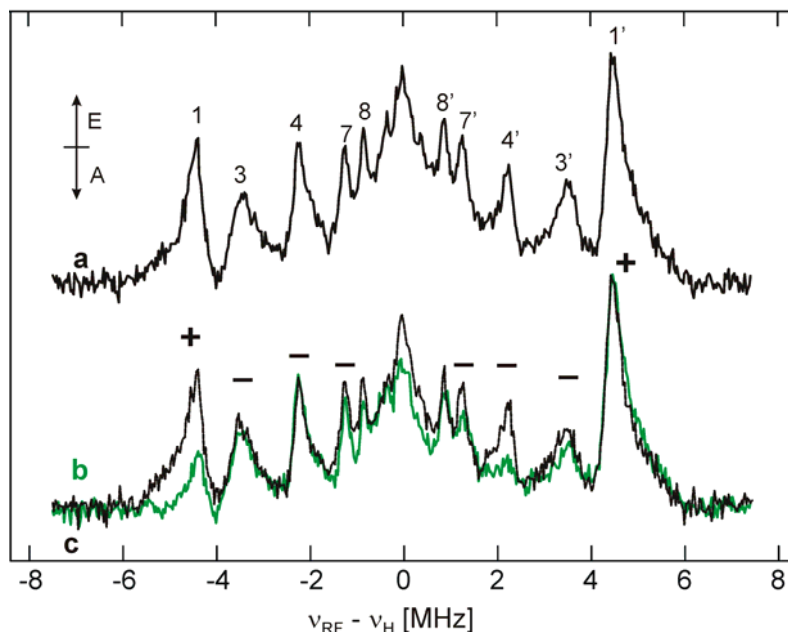


Figure S5. Variable mixing time (VMT) pulse Q-band ¹H ENDOR spectra recorded at the low field edge (close to g_x spectral position) on the RP of PS I from *Synechocystis menB26* substituted with VK₃-h₈ (T = 80 K). **(a)** Standard Davies ENDOR spectrum recorded with $t_{\text{DAF}} = 1 \mu\text{s}$ and a delay of $3 \mu\text{s}$ between the end of the RF pulse and the detection sequence ($t_{\text{DD}} = 14 \mu\text{s}$). **(b)** Green spectrum: VMT ENDOR spectrum recorded with $t_{\text{DAF}} = 1 \mu\text{s}$ and a delay of $43 \mu\text{s}$ (t_{mix}) between the end of the RF pulse and the detection sequence ($t_{\text{DD}} = 54 \mu\text{s}$). **(c)** Black spectrum: Davies ENDOR spectrum recorded with $41 \mu\text{s}$ DAF and a delay of $3 \mu\text{s}$ between the end of the RF pulse and the detection sequence ($t_{\text{DD}} = 54 \mu\text{s}$).

It was confirmed for VK₃-h₈ substituted in *Synechocystis menB26* PS I that the line pair 1/1' assigned to the methyl group protons has a positive hfc. The line pair 3/3' is associated with a negative hfc, but the response is quite weak. This might be due to different relaxation times. The line pair 4/4' shows a strong response, typical for a negative hfc. The hfc associated with line pair 7/7' is negative, too. For the signals associated with smaller hfc's no clear effect was observed.

In *Synechocystis menB26* PS I substituted with VK₃-d₈ the line pair 2, 2' was found to arise from a proton with a positive hfc. The VMT ENDOR effect of the line pairs 6/6' and

8/8' indicates for both a positive sign. It is important to note, that the positive hfc signs exclude the possibility that one of these ENDOR lines is due to the A_{\perp} component of the H-bond proton. The analysis of the smaller hfcs is complicated since the observed effects are rather small.

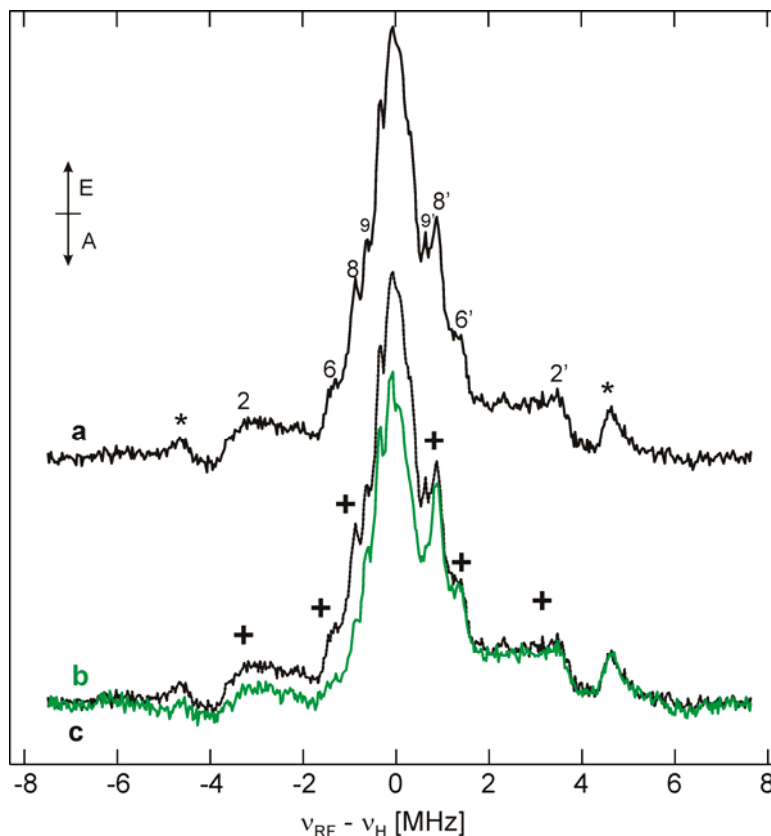


Figure S6. Variable mixing time (VMT) pulse Q-band ^1H ENDOR spectra recorded at the low field edge (close to the g_x spectral position) on the RP of PS I from *Synechocystis menB26* substituted with $\text{VK}_3\text{-d}_8$ ($T = 80\text{ K}$). (a) Standard Davies ENDOR spectrum recorded with $t_{\text{DAF}} = 1\text{ }\mu\text{s}$ and a delay of $3\text{ }\mu\text{s}$ between the end of the RF pulse and the detection sequence ($t_{\text{DD}} = 14\text{ }\mu\text{s}$). (b) **Green spectrum:** VMT ENDOR spectrum recorded with $t_{\text{DAF}} = 1\text{ }\mu\text{s}$ and a delay of $43\text{ }\mu\text{s}$ (t_{mix}) between the end of the RF pulse and the detection sequence ($t_{\text{DD}} = 54\text{ }\mu\text{s}$). (c) Black spectrum: Overlay of spectrum a.

TRIPLE measurements

In order to determine the signs of the hfcs in photoaccumulated $A_1^{\bullet-}$, electron-nuclear-nuclear TRIPLE resonance was used. Figure S7 presents the ENDOR and one-dimensional (1D) difference TRIPLE spectra of the photoaccumulated radical anion $A_1^{\bullet-}$, recorded at two different spectral positions.

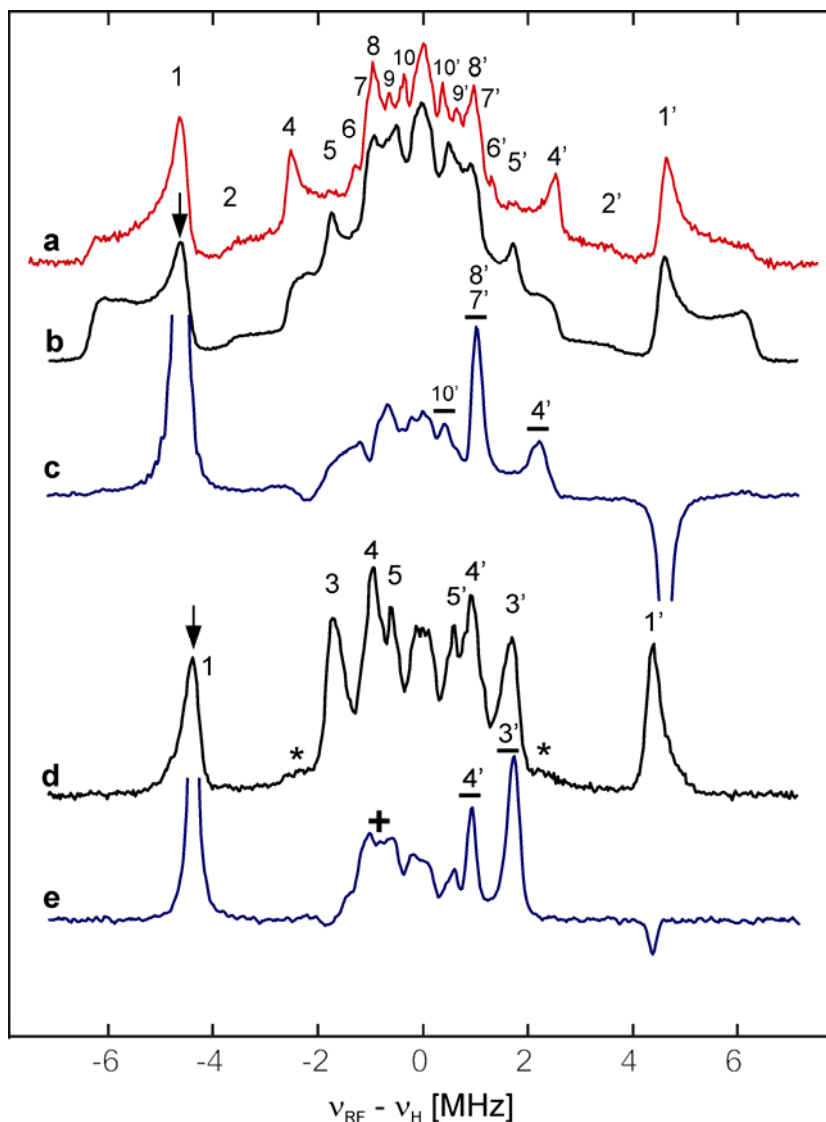


Figure S7. Pulse Q-band ^1H ENDOR spectra (black) and one-dimensional difference TRIPLE spectra (blue) recorded on $A_1^{\bullet-}$ in *T. elongatus* PS I at two different spectral positions, g_x to g_y (spectra (b) and (c)) and close to g_z (spectra (d) and (e)) at 80 K. The pulse ENDOR spectrum recorded at the low field edge ($g > g_x$; red spectrum (a)) is also shown. The arrows mark the RF pumping frequency (low frequency ENDOR transition of the methyl group protons). The asterisks mark ENDOR lines which are due to the contaminating radical anion $A_0^{\bullet-}$ (see discussion above).

The low frequency ENDOR transition of the methyl group protons was used in both cases as the pumping frequency (marked with an arrow), since it is well separated from the other ENDOR lines and its hfc sign is known. Since the methyl group proton hfc is positive, signals from other positive hfcs are expected to be visible in the low frequency region of the ENDOR spectrum ($\nu_{\text{RF}} < \nu_{\text{H}}$), while negative hfcs will be observed in the high frequency region of the ENDOR spectrum ($\nu_{\text{RF}} > \nu_{\text{H}}$). At the g_z spectral position, a single crystal type ENDOR spectrum is observed (ENDOR spectrum **(d)**, difference TRIPLE spectrum **(e)**). The two lines 3' and 4' show a strong response in the high frequency region, hence it is concluded that both hfcs have negative signs. In the low frequency part of the spectrum a broad signal with a hfc of $\sim +1.6$ MHz is observed. Surprisingly at first glance, emissive features are observed. This is not a special feature of the difference TRIPLE spectra of $\text{A}_1^{\bullet-}$, but has been also observed for the quinone radical anions in organic solvent (data not shown) and in other systems.^{5;75;76} This “indirect TRIPLE effect” has been explained in terms of relaxation processes during the time interval used between inversion and detection.^{5;75;76}

In the difference TRIPLE spectrum recorded close to the g_x orientation **(c)**, the orientation selection in the EPR spectrum is worse, as can be seen from the powder ENDOR pattern of the methyl group hfc tensor. However, a further orientation selection is achieved in the difference TRIPLE spectrum, since the narrow RF pumping π -pulse excites more molecules close to g_x spectral position. Hence, an ENDOR spectrum recorded at the low field edge (spectrum **a**) is shown to facilitate the comparison.

The broad line pair 2/2' shows no clear response, while line pair 4/4' shows the behavior typical for protons with negative hfcs. A very strong response is observed from the sum of the line pairs 7/7' and 8/8'. Both have negative hfc. Also line pair 10/10' arises from a

proton with a negative hfc. These results agree nicely with the VMT ENDOR experiments described above.

DFT calculations

The asymmetric H-bonding of the quinone has a drastic effect on the calculated spin populations of the carbon and oxygen atoms involved as compared to a symmetric H-bonding situation (e.g. in frozen 2-propanol solution). The spin populations for $\text{VK}_1^{\bullet-}$ and $\text{VK}_3^{\bullet-}$ are given in Table S2. The shifts of spin densities are also reflected in the hfcs of the respective carbon (^{13}C) and oxygen (^{17}O) atoms (Tables S3-S6). The DFT calculations performed using COSMO⁴⁷ delivered results in close agreement with the ones presented below (data not shown).

Table S2: Comparison of calculated Mulliken spin populations of the (ring) carbon and oxygen atoms in $\text{VK}_1^{\bullet-}$ (truncated phytyl chain) and in $\text{VK}_3^{\bullet-}$ in the A_1 binding site of PS I (hydrogen bonded by peptide nitrogen of leucine PsaA-L722) and in organic solvents (hydrogen bonded to four 2-propanol molecules).² The numbering follows Figure1 and S1.

		O ₁	O ₄	C ₁	C ₂	C ₃	C ₄	C ₅	C ₆	C ₇	C ₈	C ₉	C ₁₀
VK₁	A₁	0.25	0.20	0.05	0.17	0.03	0.16	0.02	0.01	0.04	-0.01	0.07	0.02
	4 IP	0.20	0.21	0.14	0.09	0.09	0.14	0.02	0.02	0.02	0.02	0.03	0.03
VK₃	A₁	0.25	0.20	0.06	0.16	0.04	0.15	0.02	0.01	0.04	-0.01	0.06	0.03
	4 IP	0.21	0.20	0.14	0.11	0.08	0.13	0.01	0.03	0.02	0.02	0.02	0.03

Table S3. Calculated ^{13}C hyperfine coupling constants (MHz) of $\text{VK}_1^{\bullet-}$ (truncated phytyl chain) in the A_1 binding site of PS I. The numbering follows Figures 1 and S1.

^{13}C atom	A_x	A_y	A_z	a_{iso}
1	-15.26	-18.98	+1.77	-10.83
2	-5.06	-4.85	+32.78	+7.62
3	-10.53	-11.34	+1.20	-6.89
4	-9.73	-12.18	+32.74	+3.61
5	-2.08	-1.15	+2.19	-0.35
6	-2.14	-1.88	+0.13	-1.30
7	-0.44	-0.10	+9.18	+2.91
8	-4.11	-2.96	-6.57	-4.55
9	-5.21	-4.79	+9.29	-0.24
10	-9.19	-8.57	-2.31	-6.69
$-\text{CH}_3$	-7.01	-5.83	-6.94	-6.59
$-\text{CH}_2-$	-2.81	-1.84	-3.03	-2.56

Table S4. Calculated ^{13}C hyperfine coupling constants of $\text{VK}_3^{\bullet-}$ in the A_1 binding site of PS I (MHz). The numbering follows Figures 1 and S1.

^{13}C atom	A_x	A_y	A_z	a_{iso}
1	-15.22	-18.98	+3.34	-10.29
2	-5.17	-4.84	+33.33	+7.77
3	-10.74	-11.6	+1.96	-6.79
4	-9.95	-12.58	+27.06	+1.51
5	-2.33	-1.39	+0.83	-0.96
6	-1.81	-1.54	+1.61	-0.58
7	-0.58	-0.19	+7.98	+2.40
8	-3.87	-2.72	-5.51	-4.03
9	-5.61	-5.14	+7.93	-0.94
10	-8.26	-7.68	-0.24	-5.395
$-\text{CH}_3$	-6.89	-5.73	-6.86	-6.49

Table S5. Calculated ^{17}O hyperfine coupling constants of $\text{VK}_1^{\bullet-}$ (truncated phytyl chain) in the A_1 binding site of PS I (MHz). The numbering follows Figures 1 and S1.

^{17}O atom	A_x	A_y	A_z	a_{iso}
1	+18.08	+17.57	-94.29	-19.55
4	+13.43	+12.69	-78.99	-17.62

Table S6. Calculated ^{17}O hyperfine coupling constants of $\text{VK}_3^{\bullet-}$ in the A_1 binding site of PS I (MHz). The numbering follows Figures 1 and S1.

^{17}O atom	A_x	A_y	A_z	a_{iso}
1	+18.79	+18.22	-95.41	+18.79
4	+14.08	+13.34	-81.22	+14.08

The molecular g -tensors were also calculated. The principal values are summarized in Table S1. While the g_y and g_z values are reasonably predicted by the DFT calculations, the typical overestimation of the g_x component of quinone radicals was found. This is due to the neglect of the environment and inherent errors in the approximate DFT approach.^{4;27-30;77-79}

There have been previous DFT calculations on the quinone in the A_1 binding site which also reported the proton hfc.^{31;69} Unfortunately, in one case the unrestricted geometry optimization resulted in a erroneous short H-bond⁶⁹, while the calculations of O'Malley³¹ were done before the crystal structure of PS I was known. Thus, in the work of O'Malley a different orientation of the phytyl chain was chosen and methyl imidazole has been selected as H-bond donor, using a different orientation than that found in the crystal structure of PS I. It is also expected that the geometry optimization performed in the present work will yield more accurate results due to the use of DFT in combination with a sophisticated basis set, while O'Malley used a semi-empirical Hamiltonian (PM3). However, those studies also found that an asymmetric H-bond produces an odd alternant distribution of the π -spin density. These effects were also reflected in the calculated proton hfc tensors. Furthermore, an increased isotropic hfc was found for the methyl group in case of asymmetric H-bonding. The results obtained in these previous works are qualitatively in line with the results presented here.

References

1. Johnson, T. W.; Zybaylov, B.; Jones, A. D.; Bittl, R.; Zech, S.; Stehlik, D.; Golbeck, J. H.; Chitnis, P. R. *J. Biol. Chem.* **2001**, 276, 39512-39521.
2. Epel, B.; Niklas, J.; Sinnecker, S.; Zimmermann, H.; Lubitz, W. *J. Phys. Chem. B* **2006**, 110, 11549-11560.
3. Vassiliev, I. R.; Antonkine, M. L.; Golbeck, J. H. *Biochim. Biophys. Acta* **2001**, 1507, 139-160.
4. Sinnecker, S.; Reijerse, E.; Neese, F.; Lubitz, W. *J. Am. Chem. Soc.* **2004**, 126, 3280-3290.
5. Silakov, A.; Reijerse, E. J.; Albracht, S. P. J.; Hatchikian, E. C.; Lubitz, W. *J. Am. Chem. Soc.* **2007**, 129, 11447-11458.
6. Sienkiewicz, A.; Smith, B. G.; Veselov, A.; Scholes, C. P. *Rev. Sci. Instrum.* **1996**, 67, 2134-2138.
7. Davies, E. R. *Phys. Lett.* **1974**, 47A, 1-2.
8. Goldfarb, D.; Epel, B.; Zimmermann, H.; Jeschke, G. *J. Magn. Res.* **2004**, 168, 75-87.
9. Epel, B.; Goldfarb, D. *J. Magn. Res.* **2000**, 146, 196-203.
10. Mehring, M.; Höfer, P.; Grupp, A. *Ber. Bunsen-Ges. Phys. Chem.* **1987**, 91, 1132-1137.
11. Epel, B.; Gromov, I.; Stoll, S.; Schweiger, A.; Goldfarb, D. *Concepts in Magnetic Resonance Part B- Magnetic Resonance Engineering* **2005**, 26B, 36-45.
12. Epel, B.; Manikandan, P.; Kroneck, P. M. H.; Goldfarb, D. *Appl. Magn. Reson.* **2001**, 21, 287-297.
13. Epel, B.; Poppl, A.; Manikandan, P.; Vega, S.; Goldfarb, D. *J. Magn. Res.* **2001**, 148, 388-397.
14. Epel, B.; Niklas, J.; Antonkine, M. L.; Lubitz, W. *Appl. Magn. Reson.* **2006**, 30, 311-327.
15. Stehlik, D.; Bock, C. H.; Thurnauer, M. C. In *Advanced EPR - Applications in Biology and Biochemistry*; Hoff, A. J. Ed. Elsevier: Amsterdam, 1989; pp. 371-403.
16. McLauchlan, K. A. In *Advanced EPR - Applications in Biology and Biochemistry*; Hoff, A. J. Ed. Elsevier: Amsterdam, 1989; pp. 345-369.
17. Levanon, H. In *Biophysical Techniques in Photosynthesis*; Ames, J. and Hoff, A. J. Eds. Kluwer Academic Publishers: Dordrecht, 1996; pp. 211-234.
18. Schweiger, A.; Jeschke, G. *Principles of pulse electron paramagnetic resonance*, Oxford University Press: New York, 2001.
19. Rist, G.; Hyde, J. S. *J. Chem. Phys.* **1970**, 52, 4633-4643.
20. Hoffman, B. M.; Martinsen, J.; Venters, R. A. *J. Magn. Res.* **1984**, 59, 110-123.
21. MatlabTM. 2004. Natick, MA, The Mathworks, Inc.
22. Stoll, S.; Schweiger, A. *J. Magn. Res.* **2005**, 177, 390-403.
23. Kandrashkin, Y. E.; Salikhov, K. M.; van der Est, A.; Stehlik, D. *Appl. Magn. Reson.* **1998**, 15, 417-447.
24. Salikhov, K. M.; Schlüpmann, J.; Plato, M.; Möbius, K. *Chem. Phys.* **1997**, 215, 23-35.
25. Kandrashkin, Y. E.; Salikhov, K. M.; Stehlik, D. *Appl. Magn. Reson.* **1997**, 12, 141-166.
26. Jordan, P.; Fromme, P.; Witt, H. T.; Klukas, O.; Saenger, W.; Krauss, N. *Nature* **2001**, 411, 909-917.
27. Kacprzak, S.; Kaupp, M.; MacMillan, F. *J. Am. Chem. Soc.* **2006**, 128, 5659-5671.
28. Asher, J. R.; Doltsinis, N. L.; Kaupp, M. *Magn. Reson. Chem.* **2005**, 43, S237-S247.
29. Asher, J. R.; Doltsinis, N. L.; Kaupp, M. *J. Am. Chem. Soc.* **2004**, 126, 9854-9861.
30. Kaupp, M.; Remenyi, C.; Vaara, J.; Malkina, O. L.; Malkin, V. G. *J. Am. Chem. Soc.* **2002**, 124, 2709-2722.
31. O'Malley, P. J. *Biochim. Biophys. Acta* **1999**, 1411, 101-113.
32. O'Malley, P. J. *J. Am. Chem. Soc.* **1998**, 120, 11732-11737.

33. O'Malley, P. J. *J. Phys. Chem. A* **1998**, *102*, 248-253.
34. O'Malley, P. J. *J. Phys. Chem. A* **1997**, *101*, 6334-6338.
35. O'Malley, P. J. *J. Phys. Chem. A* **1997**, *101*, 9813-9817.
36. Lee, C. T.; Yang, W. T.; Parr, R. G. *Physical Review B* **1988**, *37*, 785-789.
37. Becke, A. D. *J. Chem. Phys.* **1993**, *98*, 5648-5652.
38. Stephens, P. J.; Devlin, F. J.; Chabalowski, C. F.; Frisch, M. J. *J. Phys. Chem.* **1994**, *98*, 11623-11627.
39. Dunning, T. H. *J. Chem. Phys.* **1970**, *53*, 2823-2833.
40. Frisch, M. J., Trucks, G. W., Schlegel, H. B., Scuseria, G. E., Robb, M. A., Cheeseman, J. R., Montgomery, Jr, Vreven, T., Kudin, K. N., Burant, J. C., Millam, J. M., Iyengar, S. S., Tomasi, J., Barone, V., Mennucci, B., Cossi, M., Scalmani, G., Rega, N., Petersson, G. A., Nakatsuji, H., Hada, M., Ehara, M., Toyota, K., Fukuda, R., Hasegawa, J., Ishida, T., Nakajima, T., Honda, Y., Kitao, O., Nakai, H., Klene, M., Li, X., Knox, J. E., Hratchian, H. P., Cross, J. B., Adamo, C., Jaramillo, J., Gomperts, R., Stratmann, R. E., Yazyev, O., Austin, A. J., Cammi, R., Pomelli, C., Ochterski, J. W., Ayala, P. Y., Morokuma, K., Voth, G. A., Salvador, P., Dannenberg, J. J., Zakrzewski, V. G., Dapprich, S., Daniels, A. D., Strain, M. C., Farkas, O., Malick, D. K., Rabuck, A. D., Raghavachari, K., Foresman, J. B., Ortiz, J. V., Cui, Q., Baboul, A. G., Clifford, S., Cioslowski, J., Stefanov, B. B., Liu, G., Liashenko, A., Piskorz, P., Komaromi, I., Martin, R. L., Fox, D. J., Keith, T., Al Laham, M. A., Peng, C. Y., Nanayakkara, A., Challacombe, M., Gill, P. M. W., Johnson, B., Chen, W., Wong, M. W., Gonzalez, C., and Pople, J. A. Gaussian 03, Revision B.01. 2003. Pittsburgh PA, Gaussian, Inc.
41. Neese, F. ORCA. An *ab initio*, Density Functional and Semiempirical Program Package. [2.4.]. 2004. Mülheim an der Ruhr, Germany, Max-Planck-Institut für Bioanorganische Chemie.
42. Barone, V. *Recent Advances in Density Functional Methods*, Chong, D. P. World Scientific Publ. Co.: Singapore: 1996
43. Neese, F. *J. Chem. Phys.* **2001**, *115*, 11080-11096.
44. Koseki, S.; Schmidt, M. W.; Gordon, M. S. *J. Phys. Chem. A* **1998**, *102*, 10430-10435.
45. Koseki, S.; Gordon, M. S.; Schmidt, M. W.; Matsunaga, N. *J. Phys. Chem.* **1995**, *99*, 12764-12772.
46. Koseki, S.; Schmidt, M. W.; Gordon, M. S. *J. Phys. Chem.* **1992**, *96*, 10768-10772.
47. Klamt, A.; Schüürmann, G. *Journal of the Chemical Society-Perkin Transactions 2* **1993**, *5*, 799-805.
48. Zech, S.; Hofbauer, W.; Kamlowksi, A.; Fromme, P.; Stehlik, D.; Lubitz, W.; Bittl, R. *J. Phys. Chem. B* **2000**, *104*, 9728-9739.
49. van der Est, A.; Prisner, T.; Bittl, R.; Fromme, P.; Lubitz, W.; Möbius, K.; Stehlik, D. *J. Phys. Chem. B* **1997**, *101*, 1437-1443.
50. MacMillan, F.; Hanley, J.; van der Weerd, L.; Knüpling, M.; Un, S.; Rutherford, A. W. *Biochemistry* **1997**, *36*, 9297-9303.
51. Teutloff, C.; Hofbauer, W.; Zech, S. G.; Stein, M.; Bittl, R.; Lubitz, W. *Appl. Magn. Reson.* **2001**, *21*, 363-379.
52. Pushkar, Y. N.; Golbeck, J. H.; Stehlik, D.; Zimmermann, H. *J. Phys. Chem. B* **2004**, *108*, 9439-9448.
53. Pushkar, Y. N.; Stehlik, D.; van Gastel, M.; Lubitz, W. *Journal of Molecular Structure* **2004**, *700*, 233-241.
54. Bonnerjea, J.; Evans, M. C. W. *FEBS Letters* **1982**, *148*, 313-316.
55. Brettel, K. *Biochim. Biophys. Acta* **1997**, *1318*, 322-373.
56. Gast, P.; Swarthoff, T.; Erbskamp, F. C. R.; Hoff, A. J. *Biochim. Biophys. Acta* **1983**, *722*, 163-175.
57. Smith, N. S.; Mansfield, R. W.; Nugent, J. H. A.; Evans, M. C. W. *Biochim. Biophys. Acta* **1987**, *892*, 331-334.
58. Rigby, S. E. J.; Muhiuddin, I. P.; Santabarbara, S.; Evans, M. C. W.; Heathcote, P. *Chem. Phys.* **2003**, *294*, 319-328.

59. Forman, A.; Davis, M. S.; Fujita, I.; Hanson, L. K.; Smidth, K. M.; Fajer, J. *Is. J. Chem.* **1981**, *21*, 265-269.
60. Fajer, J.; Davis, M. S.; Forman, A.; Klimov, V. V.; Dolan, E.; Ke, B. *J. Am. Chem. Soc.* **1980**, *102*, 7143-7145.
61. Lubitz W. In *Chlorophylls*; Scheer, H. Ed. CRC Press: Boca Raton, 1991; pp. 903-944.
62. Yang, F.; Shen, G. Z.; Schluchter, W. M.; Zybailov, B. L.; Ganago, A. O.; Vassiliev, I. R.; Bryant, D. A.; Golbeck, J. H. *J. Phys. Chem. B* **1998**, *102*, 8288-8299.
63. Khuzeeva, L.; Antonkine, M. L.; Niklas, J.; van der Est, A.; Lubitz, W. *in preparation* **2009**.
64. Zybailov, B.; van der Est, A.; Zech, S. G.; Teutloff, C.; Johnson, T. W.; Shen, G. Z.; Bittl, R.; Stehlik, D.; Chitnis, P. R.; Golbeck, J. H. *J. Biol. Chem.* **2000**, *275*, 8531-8539.
65. Fairclough, W. V.; Forsyth, A.; Evans, M. C. W.; Rigby, S. E. J.; Purton, S.; Heathcote, P. *Biochim. Biophys. Acta* **2003**, *1606*, 43-55.
66. Rigby, S. E. J.; Muhiuddin, I. P.; Evans, M. C. W.; Purton, S.; Heathcote, P. *Biochim. Biophys. Acta* **2002**, *1556*, 13-20.
67. Purton, S.; Stevens, D. R.; Muhiuddin, I. P.; Evans, M. C. W.; Carter, S.; Rigby, S. E. J.; Heathcote, P. *Biochemistry* **2001**, *40*, 2167-2175.
68. Rigby, S. E. J.; Evans, M. C. W.; Heathcote, P. *Biochemistry* **1996**, *35*, 6651-6656.
69. Teutloff, C. Untersuchungen zur Bindung des sekundären Akzeptors in Photosystem I mit Methoden der EPR-Spektroskopie. Doctoral Thesis, Technische Universität Berlin, Berlin, Germany 2004.
70. Teutloff, C.; Bittl, R.; Lubitz, W. *Appl. Magn. Reson.* **2004**, *26*, 5-21.
71. Hore P. J. In *Advanced EPR - Applications in Biology and Biochemistry*; Hoff, A. J. Ed. Elsevier: Amsterdam, 1989; pp. 405-440.
72. Stehlik, D.; Bock, C. H.; Petersen, J. *J. Phys. Chem.* **1989**, *93*, 1612-1619.
73. Timmel, C. R.; Fursman, C. E.; Hoff, A. J.; Hore, P. J. *Chem. Phys.* **1998**, *226*, 271-283.
74. van Dijk, B.; Gast, P.; Hoff, A. J.; Dzuba, S. A. *J. Phys. Chem. A* **1997**, *101*, 719-724.
75. Höfer, P. Entwicklung von Puls-ENDOR-Verfahren und Ihre Anwendung auf Polyazetylen. Doctoral Thesis, Universität Stuttgart, Stuttgart, Germany 1988.
76. Silakov, A. Investigation of the active site of the [FeFe] hydrogenase from *Desulfovibrio desulfuricans*. Doctoral Thesis, Heinrich-Heine-Universität Düsseldorf, Düsseldorf, Germany, 2007.
77. Kacprzak, S.; Kaupp, M. *J. Phys. Chem. B* **2004**, *108*, 2464-2469.
78. Ciofini, I.; Reviakine, R.; Arbuznikov, A.; Kaupp, M. *Theoretical Chemistry Accounts* **2004**, *111*, 132-140.
79. Kaupp, M. *Biochemistry* **2002**, *41*, 2895-2900.